PHYSICS OF FLUIDS **19**, 054106 (2007)

An intrinsic stabilization scheme for proper orthogonal decomposition based low-dimensional models

Virginia L. Kalb[a)]
NASA Goddard Space Flight Center, Greenbelt, Maryland 20771

Anil E. Deane[b)]
University of Maryland, College Park, Maryland 20742

(Received 17 June 2006; accepted 1 March 2007; published online 16 May 2007)

Despite the temporal and spatial complexity of common fluid flows, model dimensionality can often be greatly reduced while both capturing and illuminating the nonlinear dynamics of the flow. This work follows the methodology of direct numerical simulation (DNS) followed by proper orthogonal decomposition (POD) of temporally sampled DNS data to derive temporal and spatial eigenfunctions. The DNS calculations use Chorin's projection scheme; two-dimensional validation and results are presented for driven cavity and square cylinder wake flows. The flow velocity is expressed as a linear combination of the spatial eigenfunctions with time-dependent coefficients. Galerkin projection of these modes onto the Navier-Stokes equations obtains a dynamical system with quadratic nonlinearity and explicit Reynolds number (Re) dependence. Truncation to retain only the most energetic modes produces a low-dimensional model for the flow at the decomposition Re. We demonstrate that although these low-dimensional models reproduce the flow dynamics, they do so with small errors in amplitude and phase, particularly in their long term dynamics. This is a generic problem with the POD dynamical system procedure and we discuss the schemes that have so far been proposed to alleviate it. We present a new stabilization algorithm, which we term *intrinsic stabilization*, that projects the error onto the POD temporal eigenfunctions, then modifies the dynamical system coefficients to significantly reduce these errors. It requires no additional information other than the POD. The premise that this method can correct the amplitude and phase errors by fine-tuning the dynamical system coefficients is verified. Its effectiveness is demonstrated with low-dimensional dynamical systems for driven cavity flow in the periodic regime, quasiperiodic flow at Re=10000, and the wake flow. While derived in a POD context, the algorithm has broader applicability, as demonstrated with the Lorenz system. © *2007 American Institute of Physics*. [DOI: 10.1063/1.2723149]

I. INTRODUCTION

One route to extracting a higher level of information from numerical or experimental data is to look for the coherent structures in the flow as identified by the proper orthogonal decomposition (POD). This decomposition represents the flow field as a linear combination of spatial and temporal basis functions derived from the statistics of the sampled flow field (snapshots). Moreover, it orders the modes by their importance in the flow reconstruction, so that significant data reduction can be achieved by neglecting the least important terms with quantifiable negligible loss in the accuracy of the representation. This process allows one to see the important structures in the flow.

A further step is needed to gain dynamical information from the POD. This can be done by first replacing the flow variables in the Navier-Stokes equations by their POD expansions, leaving the Reynolds number (Re) as a parameter. A Galerkin projection onto the spatial basis functions results in a set of ordinary differential equations representing a dynamical system whose solution at the Reynolds number of simulation is a model of the dynamics of full DNS simulation. It is practical and convenient to truncate this model to obtain a low-dimensional system. The degree to which this system's dynamics reproduce the original time-dependence is a measure of the low-dimensional model's fidelity and usefulness.

It is of further interest for this model to reproduce the dynamics of the full system *away* from the decomposition Reynolds number, for such a valid model would allow predictions of flow behavior in regimes where no DNS has been performed. Thus much more information can be obtained by doing a parameter continuation based on the Reynolds number (Re). This is the key to investigating flow transitions since now they are equivalent to bifurcation phenomena in the dynamical system. However, one impediment to this goal is the failure of the dynamical system to exhibit the correct asymptotic behavior even at the modeled Reynolds number. Holmes *et al.*[1] note several probable causes for this deficiency:

[a)]Electronic mail: Virginia.L.Kalb@nasa.gov
[b)]Present address: Office of Advanced Scientific Computing Research, U.S. Department of Energy SC-21.1, Germantown Building, 1000 Independence Avenue SW, Washington, DC 20585. Electronic mail: Deane@ipst.umd.edu

- loss of the natural energy cascade due to low-dimensional truncation,
- numerical error in the dynamical system coefficients, particularly those involving derivatives,
- neglect of boundary or pressure terms in the computation of the dynamical system coefficients (problem and domain dependent), and
- an incomplete basis as another consequence of truncation which implies that only velocity fields close to the spatial structures of the ensemble average will be reproduced well.

The impact of the last point on the validity of the dynamical system has been addressed by Rempfer,[2] and others have sought to augment the POD spatial basis to attain better representation, e.g., Bangia *et al.*[3] and Jørgensen *et al.*[4] In particular, the unstable steady flow field might not be adequately represented by the POD spatial basis, hence not a solution of the derived dynamical system. Noack *et al.*[5] have shown that the addition of a mean-shift mode is a means of stabilizing the derived dynamical system and compensating for missing phase space directions.

In contrast, we present a means to improve the accuracy and stability of the dynamical system itself without directly addressing the source of the error. This is possible by recognizing that the POD process can provide a low-dimensional representation of the flow that is consistent with DNS, and that it also gives us the correct solution of the derived dynamical system for the initial conditions consistent with the snapshots, the temporal eigenfunctions (unnormalized). This allows us to adjust the computed coefficients so that time integration of the dynamical system does reproduce the correct solution.[6] We do not claim that this is sufficient for all purposes; in particular, it is not sufficient for parameter continuation in Reynolds number in and of itself. However, we demonstrate here that it is sufficient to capture the correct asymptotic behavior exhibited by the DNS. This is a necessary first step before gaining validity over a range of Reynolds numbers.

In this work we systematically go through the POD procedure for some test problems and demonstrate the viability of this new approach to obtain robust low-dimensional models at the Reynolds number of decomposition. Moreover, an example with the Lorenz system shows that this technique may be extended to a dynamical system obtained by Galerkin projection on any set of orthogonal basis functions with appropriate changes in the implementation.

The broad area of POD research has been active since Lumley introduced the application of POD to the study of turbulence in the late 1960s.[7] Coherent structures have long been observed in turbulent flow experiments, such as the Von Kármán vortex street behind a circular cylinder where it originates in the laminar flow regime and persists well into turbulent regime. Numerous papers attest to the success of low-dimensional models based on POD for many fluid flow problems. A comprehensive review of work in this field as well as a complete explanation of the techniques involved can be found in Holmes *et al.*[1]

Finding the optimal basis for a linear decomposition of a data set is relevant to many fields in mathematics and science. The Karhunen-Loève method was initially proposed (independently) by Karhunen[8] in 1946 and Loève[9] in 1955. The method is known by different names depending on the field of study.[10] For example, principal component analysis, proper orthogonal decomposition, empirical eigenfunction decomposition, and singular value decomposition are a few of the alternate names for equivalent procedures. It continues to be a viable topic for research and application.[11,12] More recently, control applications have utilized the POD for the creation of low order models that capture the nonlinear dynamics of the flow.[13,14]

The POD has also been used as a nonlinear dynamics tool applied to nonturbulent flow regimes to extract the spatial and temporal characteristics of the flow. When the POD is applied to a spatiotemporal data set of an evolving flow, it simultaneously derives spatial and temporal orthogonal modes which are coupled. This bi-orthogonality was noted by Sirovich[15] and highlighted by Aubry,[16] and can be mathematically defined as the representation of a flow field $\mathbf{u}(\mathbf{x},t)$ in terms of basis functions $\theta_i(t)$ and $\mathbf{\Phi}_i(\mathbf{x})$ such that

$$\mathbf{u}(\mathbf{x},t) = \sum_i \lambda_i \theta_i(t) \mathbf{\Phi}_i(\mathbf{x}),$$

with

$$\lambda_1 \geqslant \lambda_2 \geqslant \cdots \geqslant 0$$

and

$$\langle \theta_i, \theta_j \rangle = \langle \mathbf{\Phi}_i, \mathbf{\Phi}_j \rangle = \delta_{ij}.$$

Typically, the orthogonality of the temporal modes is ignored since the main objective is the dynamical system based on the spatial modes. However, this property is used to our advantage in the present work.

The first paper to apply these tools to flows in complex geometries was Deane *et al.*[17] That paper constructed low-dimensional models for flow in a periodically grooved channel and for flow past a circular cylinder. Two-dimensional simulations yield a steady flow which gives way to a periodic flow at a critical Reynolds number specific to the problem. Both flows were studied in the periodic regime and both proved amenable to representation via low-dimensional models at the Reynolds number simulated although the long-term dynamics of both systems were found to suffer from some amplitude errors even though the system remained in a stable limit cycle. Also, the four-mode dynamical system for the circular cylinder was unstable, even though four modes captures over 99% of the energy. A far more difficult problem also tackled in the Deane *et al.* paper, however, was predicting the flow properties for a range of Reynolds numbers from the models. They concluded that low-dimensional models of bounded flows such as the grooved channel flow performed better than those of open flows such as the cylinder wake in regimes away from the decomposition Reynolds numbers. The latter was found to be wholly inadequate.

Parameter continuation of these low-dimensional models remains a challenge. This work addresses one of the major obstacles to its success, viz. sufficient accuracy in the low-dimensional model. If the long-term dynamics are not captured at the modeled parameter there is little hope of accurate prediction of flow dynamics at nearby values. Two two-dimensional test flows are considered in detail: square driven cavity flow and flow past a square cylinder. The driven cavity flow is a well-studied flow with rich dynamical behavior and certain features such as its relatively unchanging mean flow make it an attractive test problem for the POD procedure. The square cylinder wake flow exemplifies bluff body wake flows with a fixed separation point (for a range of Reynolds numbers, up to 100, Ref. 18). This in turn implies little change in the distribution of pressure in that range.[19] These factors help to isolate the changes in the wake flow as the Reynolds number increases.

The recent work by Cazemier *et al.*[20] derived a low-dimensional model for the two-dimensional driven cavity flow at Re=22000, where the flow appears to be chaotic. Their 80-dimensional dynamical system was studied in depth and a bifurcation diagram was presented. The transitions of the dynamical system in the Reynolds number range 8000–12000 were compared with their DNS results. While agreement is good, the bifurcation diagram contains complicated transitions that were unconfirmed by their DNS results. In fact, there is little consensus in the literature about the flow transitions.

The paper is organized as follows: We proceed by describing our numerical approach which implements the Chorin projection method[21] on a staggered grid in the next section. A lack of accuracy here can cascade through the procedures, so comparisons with known results are presented. The next section applies the POD procedure to obtain the modes and the subsequent low-order models for the driven cavity flow and the square cylinder wake flow. Since the dynamical system must neglect higher order modes, it typically needs some sort of closure or stabilization method to accurately evolve the number of steps needed for parameter continuation. The central thrust of this work is the introduction of a new stabilization method which we term *intrinsic stabilization*[6] which exploits the bi-orthogonality of the POD. We present the approach and demonstrate its usefulness in Sec. IV. Section V provides verification of the premise that the method can correct for significant errors in the dynamical system coefficients, including phase and amplitude. We conclude with a discussion of the import of this approach on the problem in Sec. VI.

II. NUMERICAL APPROACH

We solve the 2D incompressible Navier Stokes equations[6] via a projection method which obtains a pressure Poisson equation. The splitting is

$$\frac{\mathbf{u}^{\star} - \mathbf{u}^{n}}{\Delta t} = -(\mathbf{u}^{n}\cdot\nabla)\mathbf{u}^{n} + \frac{1}{\mathrm{Re}}\Delta\mathbf{u}^{n}, \tag{1}$$

$$\Delta p^{n+1} = \frac{1}{\Delta t}\nabla\cdot\mathbf{u}^{\star}, \tag{2}$$

$$\frac{\mathbf{u}^{n+1} - \mathbf{u}^{\star}}{\Delta t} = -\nabla p^{n+1}, \tag{3}$$

where the symbols have their usual meaning. The pressure field is determined from the Poisson equation (2) with homogeneous Neumann boundary conditions.[22] For a finite difference solution, this method works best on a staggered grid where pressure is defined at the grid points, u is offset in y by $\Delta y/2$ and v is offset in x by $\Delta x/2$. The spatial discretization is overall second order, with third order handling of the nonlinear terms for the wake flow. An advantage of this splitting method is that it does not require external boundary conditions for pressure. This method has its origins in the marker and cell (MAC) method developed in 1965[23] which featured the staggered grid and a Poisson equation for pressure. The projection method coincides with the MAC method in the interior of the domain, but differs on the boundary. Many variants of these methods have been successfully used, e.g., Kim and Moin.[24]

The Poisson equation is solved using the Fourier spectral method because of its speed and ease of implementation. It is also ideal for the uniform staggered grid and otherwise second-order discretization. On a staggered grid with Neumann boundary conditions, the pressure Poisson equation can be very efficiently solved using the quarter cosine-wave transform.

Three types of boundary conditions have been implemented for this work:

- Dirichlet boundary conditions are used for prescribed inflow conditions and for the wake flow horizontal boundaries. For inflow, u values are on the boundary and are set to the desired value. The u values do not lie on the horizontal boundaries, however, boundary values are set such that the average across the boundary is the desired value. It should be noted that it is also common to use free slip ($du/dy=0$, $v=0$) on the horizontal wake boundaries. Given a sufficiently large computational domain, this is not to be a significant factor and the Dirichlet formulation is more compatible for ingest into the POD to ensure that the boundary terms are incorporated into the mean flow.
- No-slip (u and v vanish at the boundary) is used for wall boundaries. This is done by setting the normal velocity component to zero (since these grid points lie on the wall), and setting the tangential velocity component to minus the value of that velocity component at the adjacent interior point (in the normal direction) so that the average value at the wall is zero.
- Outflow (the outflowing mass flux should equal the inflowing mass flux) is needed for channel, wake, and step flows. The common method of implementing outflow by specifying zero normal gradient in u and v is fine for steady flows, but was not found to be satisfactory for unsteady wake flows. The simple device of linearly extrapolating u and v to the outflow boundary preserves the vortical structure in the wake flow and does a fine job of conserving mass flux.

The square cylinder wake flow domain is split into rectangular regions necessary for the solution of the Poisson equation for pressure by transform methods with a straight-

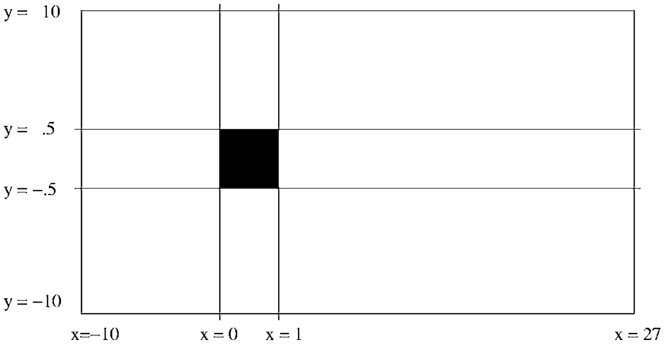

FIG. 1. Cartesian coordinates of the computational domain for the flow past a square cylinder (not to scale).

forward implementation of the alternating Schwarz method. This decomposition assures physical boundary conditions on three of the four sides for each domain. The domain in Fig. 1 was used $(\Delta x = \Delta y = \frac{1}{32})$. Figure 2 illustrates typical flow fields for periodic wake flow.

The 2D square driven cavity flow is an important benchmarking problem with a simple spatial geometry and easily implemented boundary conditions: no-slip on the three walls and a driven top edge at constant unit velocity. A common feature of nonturbulent two-dimensional driven cavity flow is a large rotating eddy occupying the central portion of the cavity. Cascades of counter-rotating eddies occupy the lower left and right corners. At high Reynolds numbers ($\geqslant 5000$), a top left eddy forms.

Extensive benchmarking results for $\mathrm{Re} \leqslant 10000$ are available from Ghia *et al.*[25] However, Ghia's work found a steady state up to $\mathrm{Re}=10000$. More recent publications (e.g., Cazemier[20]), and our results suggest that the flow in fact undergoes two bifurcations before $\mathrm{Re}=10000$. For this reason, the benchmarking results presented here are restricted to steady flow. Grid refinement has been done for key unsteady driven cavity flows at Reynolds numbers 8500 and 10000 to validate the later results (Figs. 3 and 4).

Ghia *et al.*[25] used a vorticity-stream function formulation of the Navier-Stokes equations with a multigrid solution method on a uniform grid of 128×128 to resolve this same flow. Second-order central differencing was used for all second-order derivatives, and upwinding for the convective terms. The multigrid technique allows local grid refinement by defining progressively finer grids in selected regions as

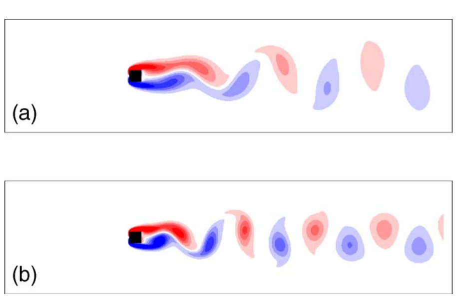

FIG. 2. (Color online) Partial view of a typical flow field for flow past a square cylinder at Re=55 (a) and Re=90 (b) showing vorticity; red=− (clockwise rotation) and blue=+ (counterclockwise).

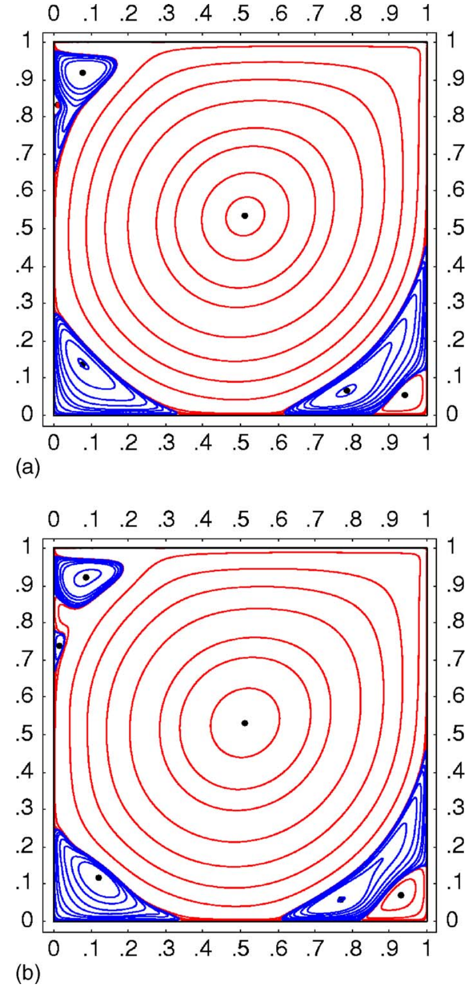

FIG. 3. (Color online) Stream function of typical flow field for the driven cavity flow at Re=8500 (a) and Re=10000 (b); red=− and blue=+. Dots mark discernible vortices.

needed. A more recent publication by Botella and Peyret[26] obtained a highly accurate solution for this flow by a Chebyshev collocation method. The velocity is approximated with a polynomial of at most degree N in both spatial directions, its values defined on the $(N+1)\times(N+1)$ Gauss-Lobatto grid. The pressure is defined as a polynomial of degree two less, and is calculated at the $(N-1)\times(N-1)$ inner nodes. The published results used for comparison here are for the highest resolution reported at $N=160$. Special attention was paid to the lid corner singularities where the velocity is discontinuous. Their boundary condition for the lid, however, was $u \equiv -1$, opposite to convention. This necessitates a mirroring of x coordinates and negating of u values for comparison with results from lid velocity $u \equiv +1$. Figure 5(a) plots the u velocity component along the vertical center line of the cavity in black. The squares show this information for the locations in Ghia *et al.*,[25] and the triangles show $-u$ for the locations in Botella *et al.*[26] Figure 5(b) shows the v velocity component along the horizontal center line of the cavity in black. The squares show this information for the locations in Ghia *et al.*,[25] and the triangles show the same for $1-x$, where x is as published in Botella *et al.*[26] Figures 6(a) and 6(b) display the same information for Re=5000 with dots for

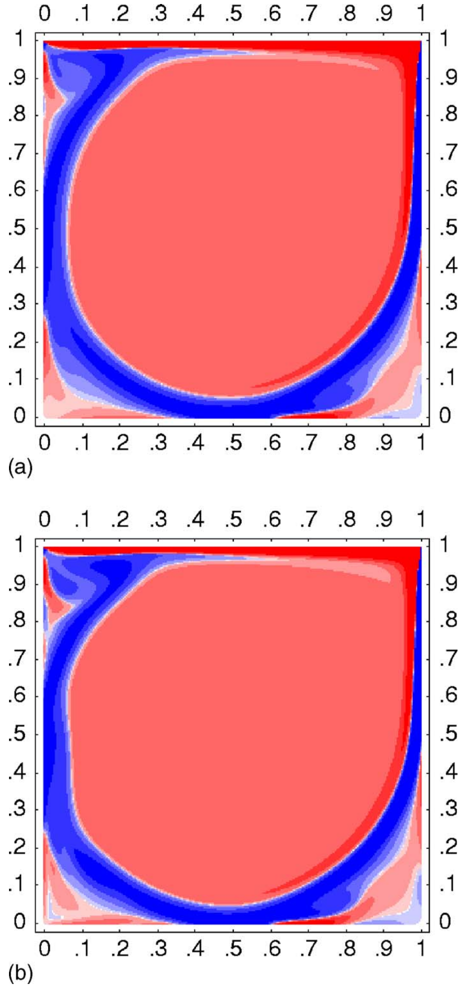

FIG. 4. (Color online) Vorticity of typical flow field for the driven cavity flow at Re=8500 (a) and Re=10000 (b); red=− (clockwise rotation) and blue=+ (counterclockwise).

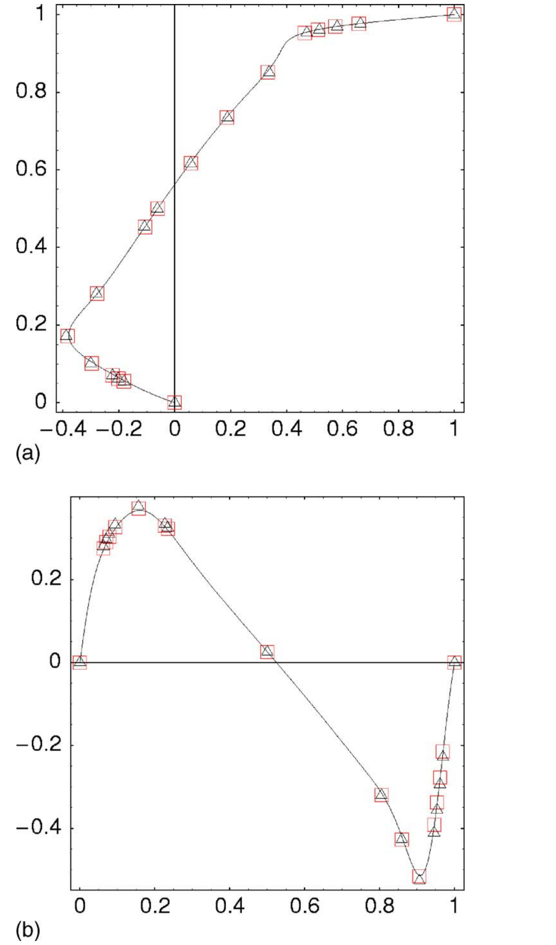

FIG. 5. (Color online) Comparison of solutions to the driven cavity flow at Re=1000: black=256×256, squares=Ghia *et al.*, triangles=Botella *et al.* (a) u along vertical center line [plotted (u,y)]; (b) v along horizontal center line [plotted (x,v)].

Ghia *et al.*[25] Finally, Figs. 7(a) and 7(b) display this information for Re=7500 with dots for Ghia *et al.*[25]

Numerous other comparisons with published calculations of L-shaped cavity Oosterlee *et al.*[27] and backwards-facing step by Gresho *et al.*[28] have been documented in Ref. 6 and convince us that the code performs adequately on the problems and parameter ranges of interest.

III. PROPER ORTHOGONAL DECOMPOSITION

The operational idea behind this method is the fact that a real symmetric nonsingular matrix $\mathbf{C}$ can be diagonalized by a special orthonormal matrix $\mathbf{W}$ such that $\mathbf{W}^T\mathbf{C}\mathbf{W}=\mathbf{D}$, where $\mathbf{D}$ is a diagonal matrix. The columns of $\mathbf{W}$ are the normalized eigenvectors of $\mathbf{C}$ and the diagonal entries of $\mathbf{D}$ are the eigenvalues of $\mathbf{C}$. Moreover, the eigenvectors form an orthogonal basis, hence are uncorrelated, thereby maximizing the information content in each and minimizing redundancy. The covariance matrix of a data set is the real symmetric matrix used for the KL procedure.

The application of the method can be considered in two ways: find the eigenstructure of the spatial covariance matrix or of the temporal covariance matrix. The eigenvalues are equivalent and there is a simple relationship between the eigenvectors of both covariance matrices, but the magnitude of the two problems is not necessarily equivalent. It is usually more tractable to use the temporal covariance matrix (of dimension $M\times M$, where M is the number of snapshots) because it is usually the case that there are many more grid points than snapshots. The ith eigenvector corresponds to the coefficients for a linear combination of snapshots to form the ith principal spatial orthogonal component. If there is redundancy in the data, the number of significant eigenvalues will be less than M, and only those corresponding eigenvectors are used, producing less than M principal components. The use of the temporal covariance matrix is known in the literature as the "snapshot" method.[15]

Details of this computation may be found in any number of references, e.g., Ref. 16 hence are omitted here. To summarize some of the important properties of the POD, given a data set $\mathbf{u}(\mathbf{x},t)$, spatial basis functions $\mathbf{B}_i(\mathbf{x})$ and corresponding temporal functions $b_i(t)$, $i=1,N$:

- The POD choice $b_i=\theta_i$ and $\mathbf{B}_i=\mathbf{\Phi}_i$ minimizes the reconstruction error $\langle\|\mathbf{u}(\mathbf{x},t)-\Sigma_{i=1}^{M}a_i(t)\mathbf{B}(\mathbf{x})\|^2\rangle$ for any level of truncation $M\leq N$; more precisely, the error is smaller than the square root of the $(M+1)$st eigenvalue,[16] where $\theta_i(t)$

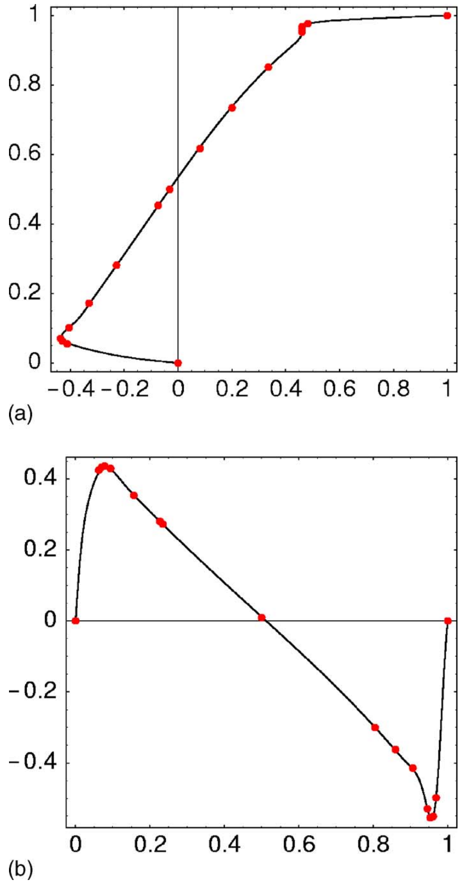

FIG. 6. (Color online) Comparison of solutions to the driven cavity flow at Re=5000: black=256×256, red dots=Ghia *et al.* (a) u along vertical center line [plotted (u,y)]; (b) v along horizontal center line [plotted (x,v)].

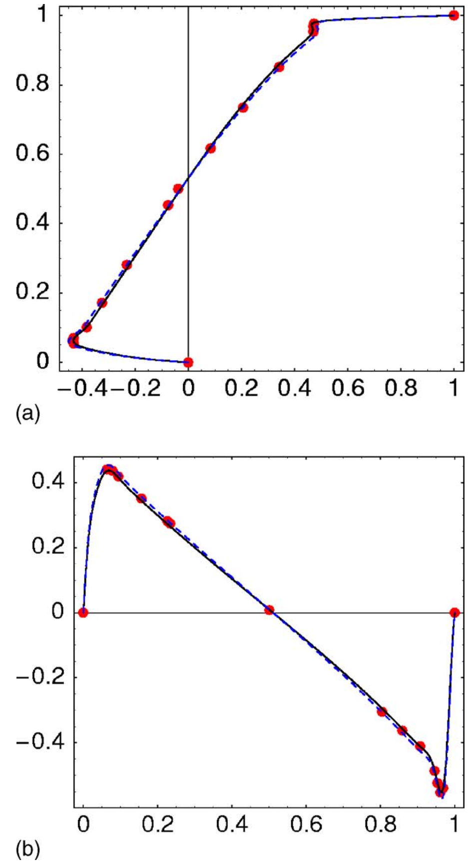

FIG. 7. (Color online) Comparison of solutions to the driven cavity flow at Re=7500: black=256×256, blue=512×512 grid, red dots=Ghia *et al.* (a) u along vertical center line [plotted (u,y)]; (b) v along horizontal center line [plotted (x,v)].

and $\mathbf{\Phi}_i$ are the ith temporal and spatial eigenfunctions, respectively.

- If $\mathbf{C}$ is the covariance matrix derived from $\mathbf{U}(\mathbf{x},t)$ with eigenvalues λ_i, $i=1,N$, then $\Sigma_{j=1}^{M}\lambda_i=\mathrm{Trace}(\mathbf{C})$ represents the average, unsteady energy in the data set and is invariant under the KL decomposition.
- λ_i is the relative energy associated with principal component i so for a given number of modes, the POD maximizes the captured energy.
- The transformation is invertible, which means that each original snapshot can be written as a linear combination of the POD components.
- In particular, if the solution vectors are divergence-free, then so are the POD components.

The spatial fields $\mathbf{\Phi}_i$ may also be interpreted as a quantitative representation of the coherent structures in the flow. The eigenvalue of each field indicates the importance of that component to the average unsteady energy of the flow. For nonturbulent flows, most of the eigenvalues are close to zero, so one can obtain a significantly simpler representation of the flow, as well as a space/time decoupling.

From the POD, we have the representation of the solution to the Navier-Stokes equation as

$$\mathbf{u}(t,\mathbf{x})=\mathbf{u}_m+\sum_{i=1}^{M}a_i(t)\mathbf{\Phi}_i(\mathbf{x}), \tag{4}$$

where $\mathbf{u}_m$ is the mean flow field and M is the number of significant "eigenfunctions" a_i (strictly speaking, a_i is not a temporal eigenfunction since in this representation, it is not normalized) and $\mathbf{\Phi}_i$.

Replacing $\mathbf{u}$ in the Navier-Stokes equations and performing a Galerkin projection onto the orthonormal spatial basis functions $\mathbf{\Phi}_k$ yields

$$\begin{aligned}\frac{da_k}{dt}=&-\langle\mathbf{\Phi}_k,(\mathbf{u}_m\cdot\nabla)\mathbf{u}_m\rangle-\left\langle\mathbf{\Phi}_k,\sum_{i=1}^{M}a_i(\mathbf{\Phi}_i\cdot\nabla)\mathbf{u}_m\right\rangle\\&-\left\langle\mathbf{\Phi}_k,\sum_{i=1}^{M}a_i(\mathbf{u}_m\cdot\nabla)\mathbf{\Phi}_i\right\rangle\\&-\left\langle\mathbf{\Phi}_k,\sum_{i=1}^{M}\sum_{j=1}^{M}a_ia_j(\mathbf{\Phi}_i\cdot\nabla)\mathbf{\Phi}_j\right\rangle-\langle\mathbf{\Phi}_k,\nabla p\rangle\\&+\left\langle\mathbf{\Phi}_k,\frac{1}{\mathrm{Re}}\nabla^2\left(\mathbf{u}_m+\sum_{i=1}^{M}a_i\mathbf{\Phi}_i\right)\right\rangle.\end{aligned}$$

The pressure term can be integrated by parts to yield

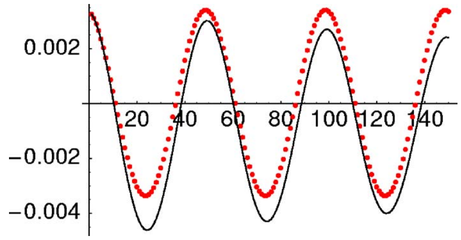

FIG. 8. (Color online) Mode 1, $a_1(t)$ and unstabilized ODE solution. Figures 8–11 refer to the low-dimensional model for driven cavity flow at Re =8500. Red dots: exact from POD; black: evolved.

$$-\langle \mathbf{\Phi}_k, \nabla p \rangle = -\langle \nabla \cdot \mathbf{\Phi}_k, p \rangle - \int_\Gamma \mathbf{\Phi}_k p.$$

The spatial basis functions $\mathbf{\Phi}_k$ are divergence-free, so the first term vanishes. The $\mathbf{\Phi}_k$ vanish on the cavity boundaries since the flow there is constant, hence equal to the mean flow. Thus, the boundary integration term is zero as well. For the flow past the square cylinder, the $\mathbf{\Phi}_k$ are likewise zero on all except the outflow boundary. At outflow, however, there is some question about the contribution from this term. In the past, the pressure has been treated as zero (e.g., Refs. 17 and 29) so again there is no contribution from the boundary term. However, this assumption demands an infinitely long domain, which is not attainable. Several authors have included contributions from this term for channel flow (Galleti *et al.*[30]) and shear flow (Noack *et al.*[31]), although Noack *et al.* have found this term to be negligible for large wake domains.[31] However depending on the problem, domain, and truncation level, neglect of this term could add to the uncertainty in the ability of the computed dynamical system to faithfully represent the actual flow dynamics. The intrinsic stabilization algorithm can correct for this potential error source as well, by modifying ("correcting") the linear term, in situations where the pressure term is adequately expressed by a linear model, e.g., channel flow.[30]

Using the orthonormality of the $\mathbf{\Phi}_k$ the dynamical system becomes (cf. Refs. 17 and 20)

$$\begin{aligned}\frac{da_k}{dt} = &-\langle \mathbf{\Phi}_k, (\mathbf{u}_m \cdot \nabla)\mathbf{u}_m \rangle - \sum_{i=1}^{N} \langle \mathbf{\Phi}_k, (\mathbf{\Phi}_i \cdot \nabla)\mathbf{u}_m \rangle a_i \\ &- \sum_{i=1}^{N} \langle \mathbf{\Phi}_k, (\mathbf{u}_m \cdot \nabla)\mathbf{\Phi}_i \rangle a_i \\ &- \sum_{i=1}^{N}\sum_{j=1}^{N} \langle \mathbf{\Phi}_k, (\mathbf{\Phi}_i \cdot \nabla)\mathbf{\Phi}_j \rangle a_i a_j + \frac{1}{\mathrm{Re}} \langle \mathbf{\Phi}_k, \nabla^2 \mathbf{u}_m \rangle \\ &+ \frac{1}{\mathrm{Re}} \sum_{i=1}^{N} \langle \mathbf{\Phi}_k, \nabla^2 \mathbf{\Phi}_i \rangle a_i \end{aligned} \tag{5}$$

$$= A_k + \sum_{i=1}^{N} B_{ki} a_i + \sum_{i=1}^{N}\sum_{j=1}^{N} C_{kij} a_i a_j, \tag{6}$$

where

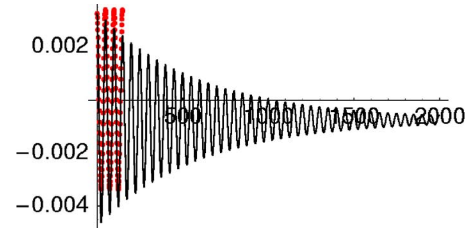

FIG. 9. (Color online) Asymptotic behavior of mode 1, $a_1(t)$ and unstabilized ODE solution. See Fig. 8 for details.

$$A_k = -\langle \mathbf{\Phi}_k, (\mathbf{u}_m \cdot \nabla)\mathbf{u}_m \rangle + \frac{1}{\mathrm{Re}} \langle \mathbf{\Phi}_k, \nabla^2 \mathbf{u}_m \rangle,$$

$$B_{ki} = -\langle \mathbf{\Phi}_k, (\mathbf{\Phi}_i \cdot \nabla)\mathbf{u}_m \rangle - \langle \mathbf{\Phi}_k, (\mathbf{u}_m \cdot \nabla)\mathbf{\Phi}_i \rangle + \frac{1}{\mathrm{Re}} \langle \mathbf{\Phi}_k, \nabla^2 \mathbf{\Phi}_i \rangle,$$

$$C_{kij} = -\langle \mathbf{\Phi}_k, (\mathbf{\Phi}_i \cdot \nabla)\mathbf{\Phi}_j \rangle.$$

From a practical consideration, it is beneficial to use integration by parts to reduce the terms involving second order derivatives to functions of first order derivatives because it is necessary to compute first order derivatives for all other terms. Since the spatial eigenfunctions are zero on the boundary, the boundary terms vanish:

$$A_k = -\langle \mathbf{\Phi}_k, (\mathbf{u}_m \cdot \nabla)\mathbf{u}_m \rangle - \frac{1}{\mathrm{Re}} \langle \nabla \mathbf{\Phi}_k, \nabla \mathbf{u}_m \rangle,$$

$$B_{ki} = -\langle \mathbf{\Phi}_k, (\mathbf{\Phi}_i \cdot \nabla)\mathbf{u}_m \rangle - \langle \mathbf{\Phi}_k, (\mathbf{u}_m \cdot \nabla)\mathbf{\Phi}_i \rangle - \frac{1}{\mathrm{Re}} \langle \nabla \mathbf{\Phi}_k, \nabla \mathbf{\Phi}_i \rangle,$$

$$C_{kij} = -\langle \mathbf{\Phi}_k, (\mathbf{\Phi}_i \cdot \nabla)\mathbf{\Phi}_j \rangle.$$

Long-term dynamics

The actual computation of these coefficients entails numerically computing first order derivatives of the mean flow field and the eigenfunctions, and many inner products. This is far from a perfect process: "There may be a significant margin of error in the coefficients, especially those involving derivatives."[1] The aforementioned pressure term may also contribute to error in the coefficients as well as the inaccuracies mentioned earlier as a consequence of truncation.

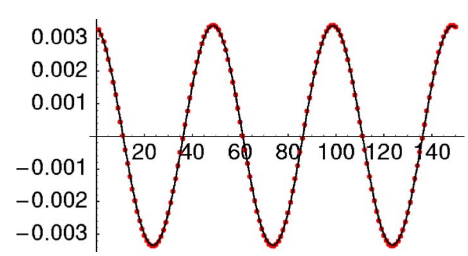

FIG. 10. (Color online) Mode 1, $a_1(t)$ and intrinsically stabilized ODE solution. See Fig. 8 for details.

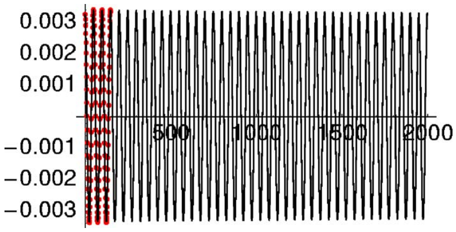

FIG. 11. (Color online) Asymptotic behavior of mode 1, $a_1(t)$ and intrinsically stabilized ODE solution. See Fig. 8 for details.

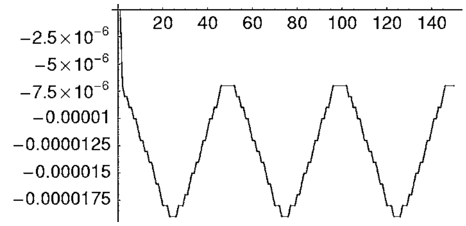

FIG. 12. Error, $\epsilon_1(t)$, for mode 1 of the driven cavity flow at Re=8500.

These errors are a significant problem, because the long term stability of the system of Eqs. (6) is at stake. We need the asymptotic behavior of these equations to accurately reflect the DNS solution, or it will be useless in a parameter continuation scenario.

Various methods have been proposed for closure or stabilization of the dynamical system under the assumption that the main problem lies with the truncation of the system. One method of stabilizing the dynamical system is nonlinear Galerkin projection[32] which was introduced specifically to address the problem of long-term integration of evolution differential equations. Given a truncated dynamical system of order M, this method seeks to incorporate the effect of the neglected higher modes on the premise that they are in fact important for asymptotic behavior. An example of this method was presented in Bangia *et al.*[3] They treat the first M modes as master modes which govern the dynamics of the flow, and the higher modes as slave modes. The equations for the slave modes are not differential equations, but algebraic equations dependent on the master modes. However, this method proves inadequate for some reduced flow systems.[33]

The Heisenberg model augments each ordinary differential equation (ODE) in Eq. (6) with a linear term μa_k where μ is a free parameter that is not determined *a priori*, but is tuned for stabilizing the integration. The idea behind this method is compensation for the loss of dissipation incurred by neglecting the higher order modes.[34]

Another strategy for dealing with nonchaotic flows is to include transient behavior to get statistical variance about the attractor (e.g., Refs. 17 and 35). However, while this may stabilize the scheme, the limit cycle amplitude obtained may be different from that obtained from the full simulation, which was the case in Ref. 17.

Cazemier[20] also proposed a dissipative closure model which would (possibly) add a linear damping term to the dynamical system. The coefficient of the new term is determined from the requirement that the energy of the new dynamical system be conserved. Using the notation of Eq. (6), the new term is D_k and $\sum_{i=1}^{M}\sum_{j=1}^{M}-C_{kij}\langle a_k(t_m)a_i(t_m)a_j(t_m)\rangle_N-(B_{kk}+D_k)\lambda_k=0$ where λ_k is the kth eigenvalue from the POD and the triple product is a temporal average. However, this factor does not always behave in the desired manner, so its inclusion is on an *ad hoc* basis.

A recently introduced stabilization scheme by Sirisup *et al.*[33] is based on the spectral vanishing viscosity (SVV) idea of Tadmor.[36] This approach adds a small amount of dissipation, decreasing with mode number, to high-frequency components of the POD. SVV is implemented by a convolution viscosity kernel parameterized by a viscosity amplitude $\epsilon=\alpha/N$, where N is the truncation level of the POD-based dynamical system, and a cut-off mode $M<N$ which determines the modes for added viscosity. The free parameters need to be determined for the specific flow problem at hand. Results are given for the periodic flow past a 2D circular cylinder in Ref. 33. However, as the authors state: "correcting the long-term behavior of the POD model does not imply that the model can correctly capture the correct bifurcation dynamics of the flow," as they demonstrate at Re=500.

The irony lies in the fact that we *a priori* know the solution to the system of differential equations [Eq. (6)] from the POD procedure: the temporal functions $a_i(t)$ [Eq. (4)]. For instance, the driven cavity flow at Re=8500 was uniformly sampled after all transients had ceased, and the POD temporal eigenfunctions are periodic as expected. Therefore, it seems reasonable to assume that the failure of the dynamical system to reproduce the temporal eigenfunctions may be attributed to the possible error sources listed in the Introduction. Thus we propose to use the known solution of Eq. (6) to adjust the coefficients so that the dynamical system can evolve the correct solution at the Reynolds number of simulation. This is explored in the next section.

IV. THE INTRINSIC STABILIZATION SCHEME

We introduce the new approach as *intrinsic stabilization* to emphasize that the information required for its implementation is known *a priori* through the POD. The key concept is the calculation of the local error incurred by use of the POD based dynamical system compared to the temporal eigenfunctions, hereafter referred to as the "true solution" of the dynamical system. Since the true solution is only known at the snapshot times, the dynamical system is reinitialized at

TABLE I. Constant coefficient, $k=1,\ldots,4$.

(A_k)	1.86476×10^{-5}	9.05858×10^{-5}	7.87272×10^{-6}	1.08822×10^{-5}
$(A_k+\alpha_k)$	5.80122×10^{-6}	-5.32830×10^{-7}	5.63856×10^{-7}	1.49441×10^{-6}

TABLE II. Linear coefficient, $j=1,\ldots,4$.

(B_{1j})	-1.66790×10^{-3}	-1.31134×10^{-1}	-1.11737×10^{-2}	-7.52489×10^{-3}
$(B_{1j}+\beta_{1j})$	6.00125×10^{-6}	-1.30911×10^{-1}	-1.15277×10^{-2}	-7.86728×10^{-3}
(B_{2j})	1.20817×10^{-1}	-1.65227×10^{-3}	-1.13540×10^{-2}	1.75379×10^{-2}
$(B_{2j}+\beta_{2j})$	1.20744×10^{-1}	1.67868×10^{-4}	-1.13201×10^{-2}	1.82748×10^{-2}
(B_{3j})	4.47706×10^{-4}	1.17824×10^{-4}	-3.08128×10^{-2}	2.74560×10^{-1}
$(B_{3j}+\beta_{3j})$	-3.50752×10^{-5}	-1.95026×10^{-4}	-3.00244×10^{-2}	2.74147×10^{-1}
(B_{4j})	-6.58169×10^{-5}	-2.60856×10^{-4}	-2.50137×10^{-1}	-2.99096×10^{-2}
$(B_{4j}+\beta_{4j})$	-1.40871×10^{-4}	1.92486×10^{-5}	-2.49200×10^{-1}	-2.96537×10^{-2}

each snapshot time to the true solution, and time-stepped to the next snapshot time. The local error is the difference between the true solution and the time-stepped solution.

Let $\mathbf{b}(t)$ be the computed solution, $\mathbf{a}(t)$ be the true solution, and $\boldsymbol{\epsilon}(t)$ be the local error function. The kth component of $\mathbf{a}(t)$, $a_k(t)$, is the kth temporal mode, and similarly $b_k(t)$ and $\epsilon_k(t)$ refer to the kth temporal mode. M is the truncation level; $M\leqslant N$, where N is the total number of snapshots. While the true solution $\mathbf{a}(t)$ theoretically satisfies our exact dynamical system, in fact we only know it as a discrete function at the snapshot times, $t=t_n$, $n=1,\ldots,N$, where $t_{n+1}=t_n+h$. It will also be useful to refer to the functions at each mode as a vector in time, e.g., $\mathbf{a}_k$ is the vector whose nth component is $a_k(t_n)$,

$$\frac{d\mathbf{a}}{dt}=G(\mathbf{a}(t)),$$

$$\frac{d\mathbf{b}}{dt}=F(\mathbf{b}(t)),$$

where G is the unknown exact dynamical system, and F is the POD based dynamical system. From the previous section,

$$\frac{db_k}{dt}=A_k+\sum_{i=1}^{M}B_{ki}b_i(t)+\sum_{i=1}^{M}\sum_{j=1}^{M}C_{kij}b_i(t)b_j(t).$$

Using a Taylor series to get a linear approximation to $\mathbf{a}(t_{n+1})$,

$$\mathbf{a}(t_{n+1})\approx\mathbf{a}(n)+\left.h\frac{d\mathbf{a}}{dt}\right|_{t_n}\approx\mathbf{a}(t_n)+hG(\mathbf{a}(t_n)).$$

Initializing the dynamical system at $t=t_n$ to $\mathbf{a}(t_n)$ and time-stepping by forward Euler,

$$\mathbf{b}(t_{n+1})\approx\mathbf{a}(t_n)+hF(\mathbf{a}(t_n)).$$

Then the local error at $t=t_{n+1}$ is

$$\boldsymbol{\epsilon}(t_{n+1})=\mathbf{a}(t_{n+1})-\mathbf{b}(t_{n+1})\approx hG(\mathbf{a}(t_n))-hF(\mathbf{a}(t_n)).$$

Using the snapshot time scale, $h=1$, but if a different time scale is used, $\boldsymbol{\epsilon}(t)$ must be scaled by h so that $\boldsymbol{\epsilon}(t_{n+1})\approx G(\mathbf{a}(t_n))-F(\mathbf{a}(t_n))$.

This information can be used to improve $\mathbf{b}$'s estimate of $\mathbf{a}$:

$$\begin{aligned}\mathbf{b}(t_{n+1})&=\mathbf{a}(t_n)+hF(\mathbf{a}(t_n))+\boldsymbol{\epsilon}(t_{n+1})\\&\approx\mathbf{a}(t_n)+h(F(\mathbf{a}(t_n))+(G(\mathbf{a}(t_n))-\ F(\mathbf{a}(t_n)))))\\&\approx\mathbf{a}(t_{n+1}).\end{aligned}$$

Incorporating this information into the dynamical system,

$$\frac{d\mathbf{b}}{dt}=F(\mathbf{b}(t))+\boldsymbol{\epsilon}(t).$$

The evolution of this intrinsically stabilized dynamical system results in a far better approximation to the true solution $\mathbf{a}$. While the formulation of the method is motivated by the use of forward Euler time-stepping, in practice it has been necessary to use a fourth order Runge-Kutta time-stepping of $\mathbf{b}$ for the calculation of the local error, $\boldsymbol{\epsilon}$. It is also feasible to time-step from $\mathbf{a}(t_n)$ to $\mathbf{b}(t_{n+1})$ on a finer time scale, but in our experience this does not improve the accuracy of the stabilized dynamical system. This is partly due to the fine sampling frequency (50 snapshots/period) used to ensure adequate bandwidth. To test this, the POD to dynamical system process was performed on the periodic flow past the square cylinder at Re=55 with 10 snapshots/period and with 5 snapshots/period. In both cases, one Runge-Kutta step proved inadequate, but two steps were sufficient. The sam-

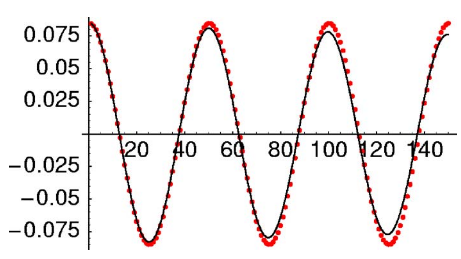

FIG. 13. (Color online) Mode 1, $a_1(t)$ and unstabilized ODE solution. Figures 13–16 refer to the low-dimensional model for flow past a square cylinder at Re=55. Red dots: exact from POD; black: evolved.

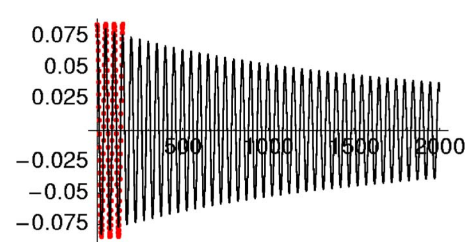

FIG. 14. (Color online) Asymptotic behavior of mode 1, $a_1(t)$ and unstabilized ODE solution. See Fig. 13 for details.

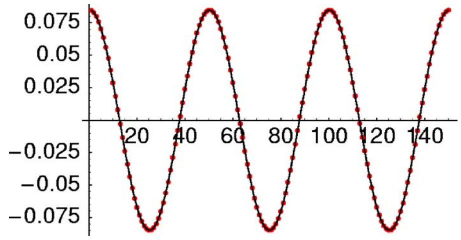

FIG. 15. (Color online) Mode 1, $a_1(t)$ and intrinsically stabilized ODE solution. See Fig. 13 for details.

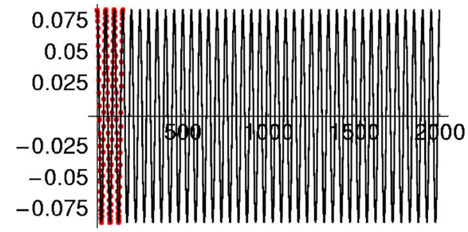

FIG. 16. (Color online) Asymptotic behavior of mode 1, $a_1(t)$ and intrinsically stabilized ODE solution. See Fig. 13 for details.

pling frequency is mandated by the temporal frequencies in the data. The Nyquist criteria, sampling frequency must be at least twice the data frequency, is a minimum criterion since we are not dealing with band-limited data, and must be calculated to accommodate the harmonics present in a nonlinear periodic flow. For the periodic flows considered here, the first pair of temporal modes corresponds to the base frequency, and modes n and $n+1$ correspond to the $n-1\text{st}/2$ harmonic. Thus, a sampling frequency of n points/period is compatible with at best an n mode dynamical system, and only then if the data are sufficiently band-limited at the highest mode so that aliasing does not interfere. For instance, the unstabilized dynamical system for the square cylinder at Re=55 sampled at 10 snapshots/period does a reasonable job of evolving the temporal eigenfunctions for an eight-mode system, but modes 9 and 10 are totally in error. Stabilization cannot change this; the information content is simply not there.

For implementation and use for determining asymptotic behavior, it is necessary for the local error function to be characterized functionally in terms of the temporal eigenfunctions $a_k(t)$. Since these functions form an orthogonal basis and assuming the computed solutions $b_k(t)$ are not grossly in error, it makes sense to project the local error $\boldsymbol{\epsilon}$ onto this basis. The mean of each mode $b_k(t)$ is not necessarily zero (as it should be), so this produces a constant term in the correction. In practice, $\boldsymbol{\epsilon}$ needs a few time steps to settle, so the correction factors are based on data from the second period (or, in the case of quasiperiodic data, mark "periods" by peaks in autocorrelation),

$$\alpha_k = \frac{\left(\sum_{i=1}^{N} \epsilon_k(i)\right)}{N},$$

$$\beta_{ki} = \frac{\langle \boldsymbol{\epsilon}_k - \alpha_k, \mathbf{a}_i \rangle}{\langle \mathbf{a}_i, \mathbf{a}_i \rangle},$$

$$\boldsymbol{\epsilon}_k \approx \alpha_k + \sum_{i=1}^{M} \beta_{ki} \mathbf{a}_i.$$

The advantage of this formulation is its ease of incorporation into the dynamical system, and the resultant form is consistent with the viewpoint of correcting the original computed dynamical system coefficients A_k and B_{ki}:

$$\frac{da_k}{dt} \approx (A_k + \alpha_k) + \sum_{i=1}^{M} (B_{ki} + \beta_{ki}) a_i(t) + \sum_{i=1}^{M} \sum_{j=1}^{M} C_{kij} a_i(t) a_j(t).$$

It should be noted that the above algorithm involves division by $\langle \mathbf{a}_i, \mathbf{a}_i \rangle$, which is essentially the square of the magnitude of the ith temporal eigenfunction, which in turn is proportional to the ith eigenvalue. The ith eigenvalue is representative of the unsteady kinetic energy is mode i, and this algorithm will fail if one attempts to extract modes past a reasonable energy cutoff. However, this may be considered as a sanity check on the number of modes used since one cannot expect information content for modes with essentially zero energy.

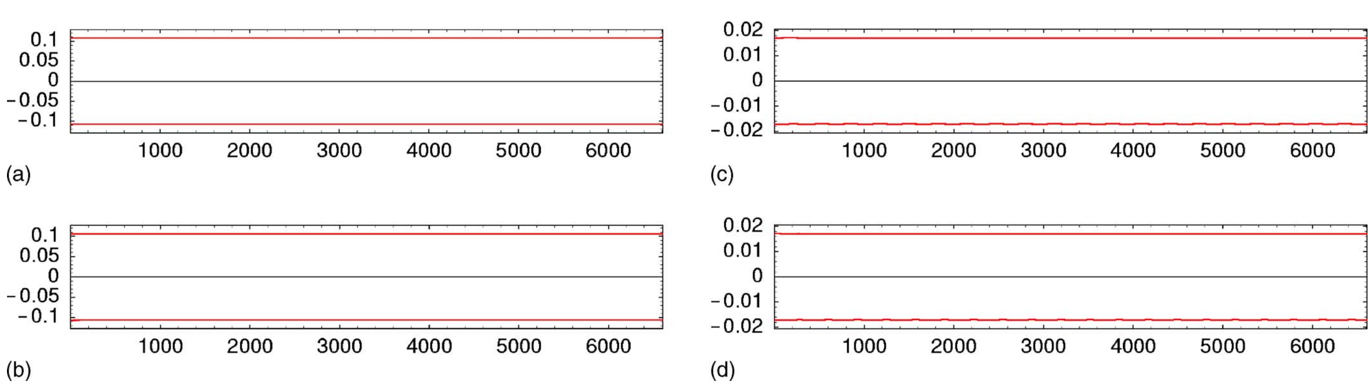

FIG. 17. (Color online) Time history of envelopes of temporal modes for a four-mode intrinsically stabilized dynamical system of flow past a square cylinder at Re=90 for 1000 shedding cycles. One shedding cycle is 6.6. (a) Mode 1; (b) mode 2; (c) mode 3; (d) mode 4.

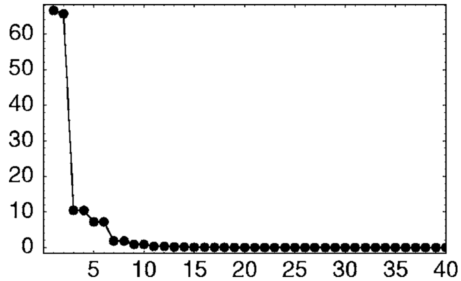

FIG. 18. Square root of eigenvalues, POD at Re=55.

The periodic flow of the driven cavity at Re=8500 illustrates the deficiency of the evolution of the unstabilized dynamical system when compared with the true temporal eigenfunctions. For this flow, virtually half of the unsteady kinetic energy is accounted for in each of the first two modes. Figure 8 shows the short term evolution of the first mode, and Fig. 9 illustrates its asymptotic behavior. Even the short term tracking is poor in this case. Figure 10 shows the effect of intrinsic stabilization for the driven cavity flow at Re=8500, and Fig. 11 illustrates its asymptotic behavior. As an example to show the magnitude of the error, Fig. 12 plots the computed error for mode 1. Tables I and II show the original and corrected dynamical system coefficients for this four-mode system. The quadratic coefficients are not changed by this algorithm. Comparison of computed versus stabilized coefficients for the four-mode dynamical system from the driven cavity flow at Re=8500.

Similarly, the first two modes for the flow past the square cylinder roughly split 95% of the kinetic energy. The short term tracking for mode 1 is quite good without any special treatment, as shown in Fig. 13, but again the asymptotic behavior (Fig. 14) could sabotage a parameter continuation effort. Intrinsic stabilization corrects this, as illustrated in Figs. 15 and 16. Moreover, the correct limit cycle behavior is obtained by this method.

Sirisup *et al.*[33] point out that a dynamical system may appear to be accurate for a certain number of shedding cycles, and then diverge. For flow past a circular cylinder at Re=100, a six-mode model with no stabilization exhibits divergence after 40 shedding cycles and a 10-mode model diverges after 500 shedding cycles. Another way of visualizing the asymptotic behavior is by plotting the maxima and minima per period for each mode versus time, thus defining the envelope of the mode. Figure 17 shows the envelopes for the four-mode intrinsically stabilized model for flow past a

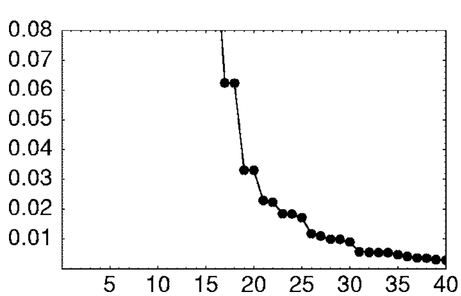

FIG. 19. Zoom of square root of eigenvalues, POD at Re=55.

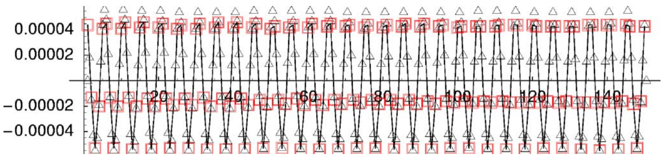

FIG. 20. (Color online) Intrinsically stabilized square cylinder wake flow, Re=55, mode 19. Red=exact from POD, black=evolved from stabilized dynamical system.

square cylinder at Re=90 for 1000 shedding cycles, showing that divergence is not a problem using this stabilization method, even for the extremely low-dimensional system of four modes which captures only 98.75% of the energy.

Are more modes better? Figures 18 and 19 show the sharp drop off of the square root of the eigenvalues (proportional to the magnitude of the corresponding temporal eigenfunction). There is a breakdown in the expected pairing of eigenvalues after the 20th eigenvalue. Even though the POD adequately resolves up to the 24th harmonic at 50 points/period, there is little information content beyond the 20th mode. The intrinsic stabilization method applied to a 20-mode dynamical system can stabilize the system and recover the correct temporal eigenfunctions. Figures 20 and 21 show recovery of the highest significant modes. The connecting plot lines are to aid interpretation, but the plot symbols show the actual data points.

Figures 22 and 23 demonstrate the correct capture of the limit cycle for the square cylinder wake flow at Re=90 by plotting the phase portraits for modes 1 versus 2 and modes 3 versus 4 for 1000 cycles of the evolved dynamical system. For comparison, the true limit cycles are plotted from the POD temporal eigenfunctions.

Figures 24–27 show a more dramatic example of the success of this procedure for the driven cavity flow for short term tracking at Re=10000 where the flow is quasiperiodic. The modes are plotted over nominally two full cycles, the time period covered by the snapshots ingested by the POD. A cycle is approximately $T=31.2$. The 16-mode low-dimensional model for this flow illustrates the ability of the intrinsic stabilization method to recover modes containing very little energy; mode 16 in Fig. 27 accounts for only 0.04% of the energy. The need for the stabilization procedure to compensate for divergence from zero mean is evident in mode 16. Another strong advantage of intrinsic stabilization over the SVV method is the fact that all modes of the model are recovered quite well. With the SVV method, after the cutoff mode inaccuracies are introduced which worsen with

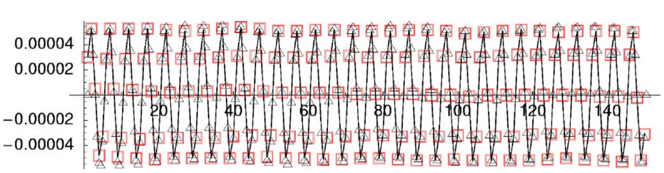

FIG. 21. (Color online) Intrinsically stabilized square cylinder wake flow, Re=55, mode 20. Red: exact from POD; black: evolved from stabilized dynamical system.

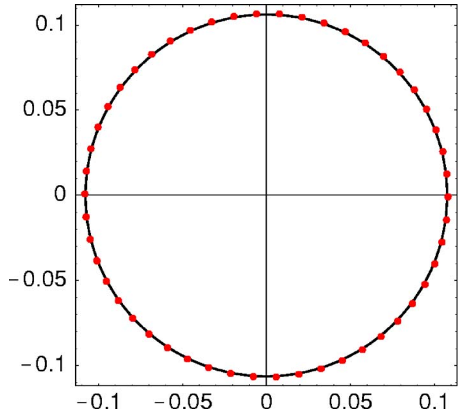

FIG. 22. (Color online) Phase portrait of modes 1 and 2. Four-mode intrinsically stabilized dynamical system of flow past a square cylinder at Re =90 for 1000 shedding cycles in black; red dots mark one cycle of corresponding temporal modes from POD.

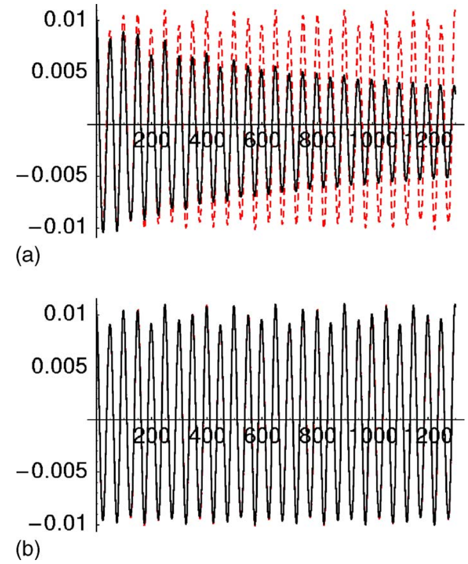

FIG. 24. (Color online) Mode 1 of 16-mode model for driven cavity flow at Re=10000. Red dashed: exact from POD; black: evolved. (a) "Raw" coefficients; (b) intrinsically stabilized.

increasing modes although the amplitude of even those modes is bounded, an improvement over no stabilization at all.[33]

The long term tracking issue raised for the four-mode model for the square cylinder is addressed for the quasiperiodic flow of the driven cavity in Figs. 28–31 which show the envelopes for the 16-mode intrinsically stabilized model for 1000 shedding cycles for modes 1, 4, 8, and 16, for brevity. We see again that divergence is not a problem using this stabilization method, even for the extremely low-energy higher modes.

While Sirisup *et al.*[33] find that correcting the long-term behavior of the POD model does not necessarily mean that the model can produce the correct bifurcation dynamics of the flow, this has not been our experience using the intrinsic stabilization method.

There is the caveat that while the qualitative bifurcation scenario is correct, the precise points of bifurcation and flow specifics at Reynolds numbers away from the decomposition Re will not be faithfully reproduced without accounting for the changes that occur in the dynamical system coefficients themselves as the Reynolds number increases, an issue addressed elsewhere.[6]

Parameter continuation using AUTO (Ref. 37) of the intrinsically stabilized dynamical system derived from the POD of the driven cavity flow at Re=8500 captures the Hopf bifurcation at Re=8446 which is consistent with the DNS. AUTO is able to follow the stable branch of periodic solutions from that bifurcation point. Similarly, continuation of the stabilized dynamical system from the POD of the square cylinder wake flow at Re=55 locates the Hopf bifurcation at Re =46 and tracks a stable periodic branch from that point, also consistent with the DNS.

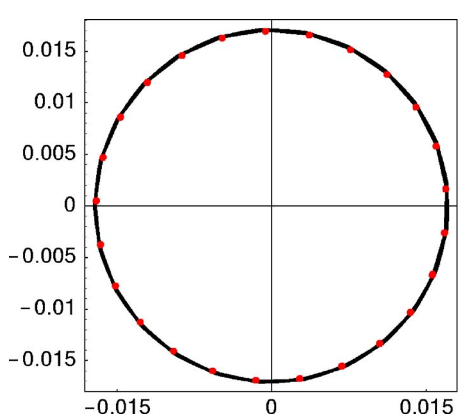

FIG. 23. (Color online) Phase portrait of modes 3 and 4. See Fig. 22 for details.

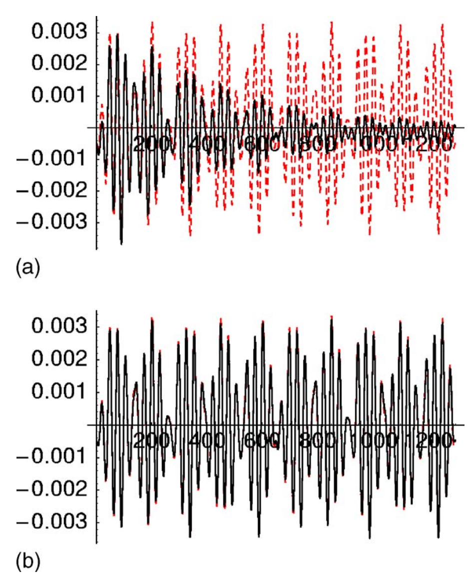

FIG. 25. (Color online) Mode 4 of 16-mode model for driven cavity flow at Re=10000. Red dashed: exact from POD; black: evolved. (a) "Raw" coefficients; (b) intrinsically stabilized.

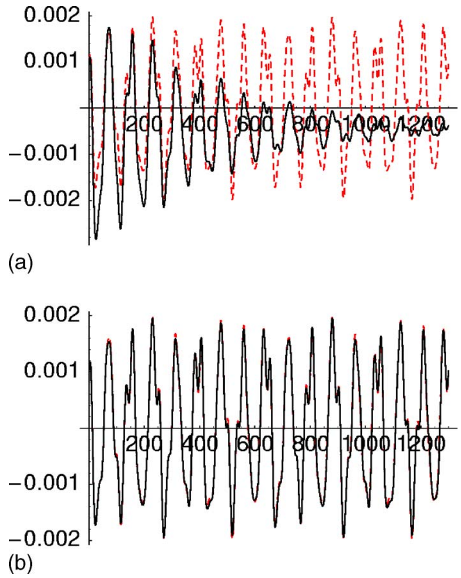

FIG. 26. (Color online) Mode 8 of 16-mode model for driven cavity flow at Re=10000. Red dashed: exact from POD; black: evolved. (a) "Raw" coefficients; (b) intrinsically stabilized.

Figure 32 illustrates parameter continuation results using AUTO (Ref. 37) for the intrinsically stabilized 16-mode dynamical system derived from the POD at Re=10000 for the driven cavity flow. The DNS shows quasiperiodic flow at that Reynolds number, and parameter continuation correctly captures first a Hopf bifurcation, then a toric bifurcation from the stable periodic branch. As noted, the specific Reynolds number of the Hopf bifurcation is off, but the qualitative bifurcation sequence agrees with the DNS. In particular, the dynamics near Re=10000 are in excellent agreement with the DNS, which finds periodic flow at Re=9900.

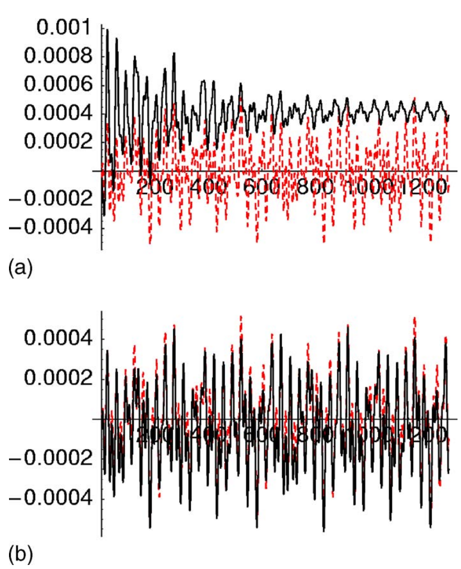

FIG. 27. (Color online) Mode 16 of 16-mode model for driven cavity flow at Re=10000. Red dashed: exact from POD; black: evolved. (a) "Raw" coefficients; (b) intrinsically stabilized.

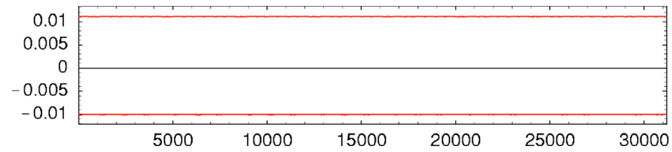

FIG. 28. (Color online) Envelope of first temporal mode for a 16-mode intrinsically stabilized dynamical system of the quasiperiodic driven cavity flow at Re=10000 for 1000 cycles. One cycle ≈31.2.

V. TEST CASES

In the previous section the intrinsic stabilization algorithm has been shown to correct for errors in the dynamical system coefficients. Examples have been shown that recover a dynamical system that correctly evolves the POD temporal functions. In the test cases considered here errors are introduced in the dynamical system coefficients that affect phase, period, and amplitude and the method is found to correct for these. Starting with the four-mode intrinsically stabilized dynamical system for the driven cavity flow at Re=8500, we perturb all of the intrinsically stabilized coefficients in three ways: add a random error to all coefficients, multiply all coefficients by a constant to shift the period, and finally divide the linear coefficients and multiply the quadratic coefficients by a constant to alter the amplitude. The evolution of the perturbed dynamical system for a 5% random error and 1% perturbation in period and amplitude is shown at the left in Figs. 33–36, along with the unperturbed evolution. Applying the intrinsic stabilization algorithm to the perturbed dynamical system yields the corrected system shown at the right in Figs. 33–36. The only caveat is good *a priori* knowledge of the true "period" (used loosely for quasiperiodic or chaotic systems, in which case substitute a statistically meaningful sampling interval), but this can be known from the DNS data before even calculating the POD, and certainly needs to be determined prior to computing the POD for adequate snapshot retrieval.

Another interesting question is how well would the algorithm work on a data set with a broader frequency spectrum. In lieu of a POD based dynamical system, we consider the Lorenz system [Eqs. (7)–(9)] which has its origins in a severely truncated model of Rayleigh-Bénard convection,[38]

$$\frac{dx}{dt} = -\sigma x + \sigma y, \tag{7}$$

$$\frac{dy}{dt} = -xz + rx - y, \tag{8}$$

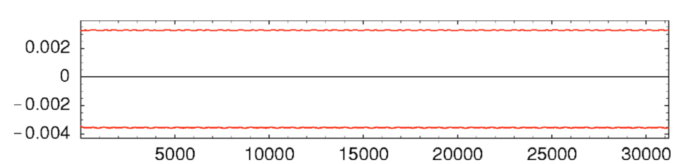

FIG. 29. (Color online) Envelope of fourth temporal mode. See Fig. 28 for details.

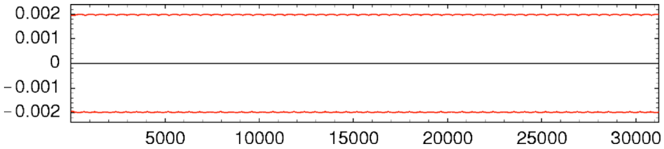

FIG. 30. (Color online) Envelope of temporal mode 8. See Fig. 28 for details.

$$\frac{dz}{dt}=xy-bz. \tag{9}$$

For this demonstration, $r=23$, $\sigma=13$, and $b=\frac{8}{3}-1$. Since this dynamical system does not arise from a POD, we do not *a priori* have a true solution. In this case, our strategy is:

- evolve a true solution for 500 time steps starting from $x0$, $y0$, $z0$;
- perturb the dynamical system coefficients σ by $+3$ and b by -1.5;
- evolve the perturbed solution starting from $x0$, $y0$, $z0$, tracking the error in x, y, and z at each step and then reinitializing to the true solution at that time step;
- use a linear regression to get the best fit for the error functions in x, y, and z (since we do not have orthogonality in this non-POD based example);
- the error functions in x, y, and z are now modeled as a constant (error mean) plus a linear combination of x, y, and z so correct the perturbed dynamical system;
- evolve the amended dynamical system and compare with the unperturbed solution; and
- do a long term (10000 steps) evolution of the corrected (perturbed then restabilized) system to see if long term agreement is achieved and compare it with the unperturbed solution.

$x0$, $y0$, and $z0$ are determined after spinning up the system for 1000 iterations from (0,1,0) to get on the attractor. Figures 37–39 contrast the unperturbed and perturbed solutions for short (500 steps) and long (10000 steps) term behavior. Figure 40 shows the $x-z$ phase portrait for the unperturbed and perturbed solutions for short and long term behavior. Figures 41–43 compare the unperturbed and corrected solutions for short (500 steps) and long (10000 steps) term behavior. Figure 44 shows the $x-z$ phase portrait for the unperturbed and corrected solutions for short and long term behavior. Although not as accurate as a linear regression with a constant term, it is simpler to report the results when the error is simply modeled as a linear combination of x, y, and z. In this case, the error functions are represented by

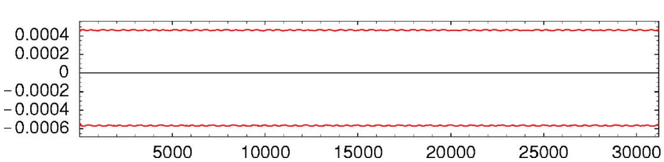

FIG. 31. (Color online) Envelope of temporal mode 16. See Fig. 28 for details.

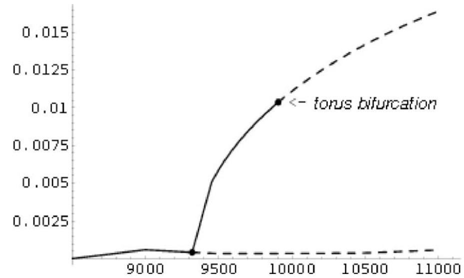

FIG. 32. L^2 norm of each mode of the parameter continuation Re of the intrinsically stabilized 16-mode dynamical system derived from the POD of the driven cavity flow at Re=10000 compared with DNS results.

$$\epsilon_x=2.75470x-2.77181y+0.000332349z,$$

$$\epsilon_y=0.247664x-0.0974575y-0.00201328z,$$

$$\epsilon_z=0.00654934x-0.00153694y-1.49961z,$$

effectively restoring the original σ and b when added to the perturbed version of Eqs. (7)–(9):

$$\begin{aligned}\frac{dx}{dt}&=-(\sigma+3)x+(\sigma+3)y+\epsilon_x\\&=-(\sigma+3-2.75470)x+(\sigma+3-2.77181)y\\&\quad+0.000332349z,\end{aligned}$$

$$\begin{aligned}\frac{dy}{dt}&=-xz+rx-y+\epsilon_y\\&=-xz+(r+.247664)x-(1.0974575)y\\&\quad-0.00201328z,\end{aligned}$$

$$\begin{aligned}\frac{dz}{dt}&=xy-(b-1.5)z+\epsilon_z\\&=xy+0.00654934x-0.00153694y\\&\quad-(b-1.5+1.49961)z.\end{aligned}$$

For a chaotic system, one cannot expect pointwise fidelity from the corrected system since the correction is linear and based on short term dynamics. However, we see in Fig. 44 that the corrected system apparently captures the correct attractor, even starting from a radically perturbed system and using relatively short term statistics. This example also gives us confidence that the method of intrinsic stabilization will work well with extended POD bases or alternative basis functions. The caveat in this example is that the sampling of the true solution must be fine enough to capture the dominant frequencies. In this example, the time step is 0.01. Basing the correction on subsampling of the true solution becomes less and less successful, until the correction fails at a subsampling of every 20 points. It should be noted that this example induces a linear error. Given that the correction is linear, this is the only type of error one could expect to correct. However, this is a consequence of the formulation of the error as a linear fit to x, y, and z. One can imagine a nonlinear error model which could address nonlinear errors.

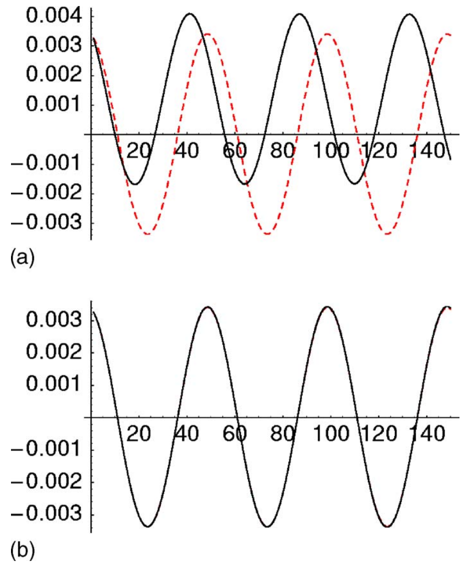

FIG. 33. (Color online) Mode 1 of four-mode model for driven cavity flow at Re=8500. Red dashed: exact from POD; black: evolved. (a) Perturbed coefficients; (b) intrinsically stabilized.

VI. CONCLUSION

We have described a stabilization scheme which is self-consistent in that it utilizes information already contained in the POD modes to arrive at low-dimensional models that more accurately describe the long-term dynamics of the full system. We have demonstrated that this accuracy is unprecedented, in that no other method proposed in the literature reproduces the accuracy of the higher-order modes with such fidelity. The method is straightforward to apply and is both conceptually as well as computationally simple.

The utility of such a stabilization, we have argued, is in our goal of using these low-dimensional models not only at the decomposition values Re but also away from this value. We will describe these results more completely elsewhere, but here we point out three salient features:

- A robust, accurate and stable (in the sense of long-term dynamics) low-dimensional system influences the bifurcation structure of the system at Re away from the decomposition value. Nonstabilized low-dimensional systems can exhibit short time dynamics, while almost-faithfully reproducing a few cycles, can nevertheless asymptotically either diverge or evolve to a limit cycle, and thus the bifurcation diagram they represent is erroneous. The initial Hopf-point may be moved and subsequent bifurcations delayed or otherwise affected. It is incumbent on the modeler to obtain as accurate a model as possible.

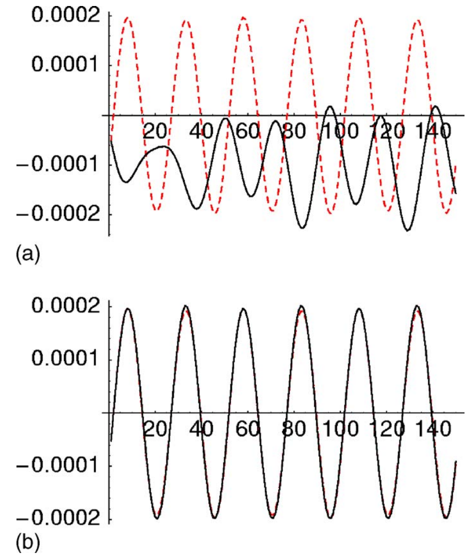

FIG. 35. (Color online) Mode 3 of four-mode model for driven cavity flow at Re=8500. Red dashed: exact from POD; black: evolved. (a) Perturbed coefficients; (b) intrinsically stabilized.

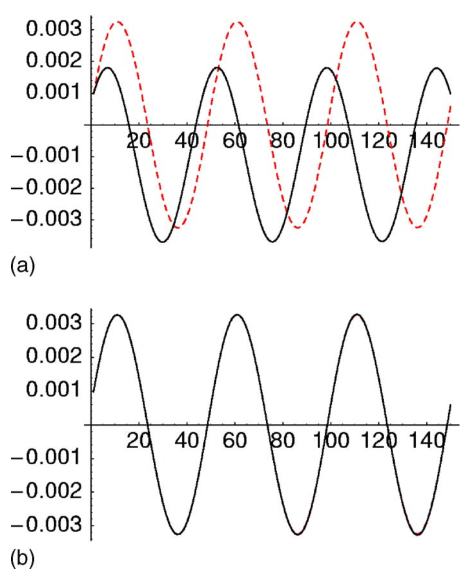

FIG. 34. (Color online) Mode 2 of four-mode model for driven cavity flow at Re=8500. Red dashed: exact from POD; black: evolved. (a) Perturbed coefficients; (b) intrinsically stabilized.

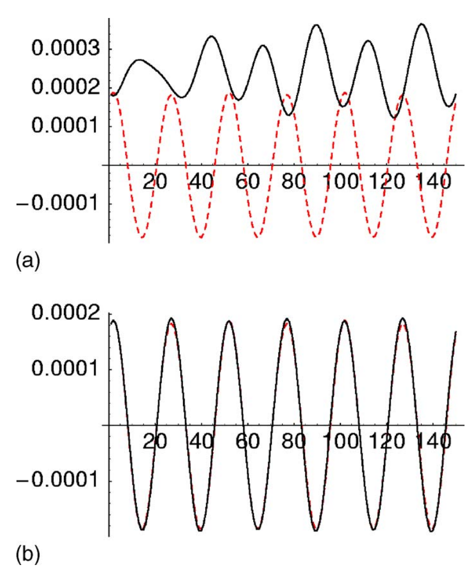

FIG. 36. (Color online) Mode 4 of four-mode model for driven cavity flow at Re=8500. Red dashed: exact from POD; black: evolved. (a) Perturbed coefficients; (b) intrinsically stabilized.

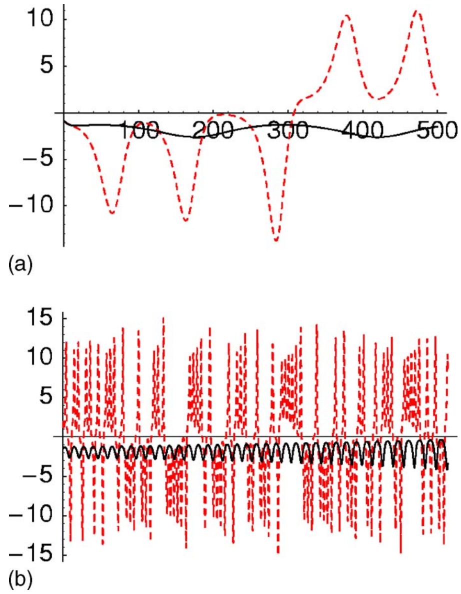

FIG. 37. (Color online) Evolution of x from Lorenz equations. Original, red dashed; perturbed, solid black. (a) Short term (500 steps), x. (b) Long term (10000 steps), x.

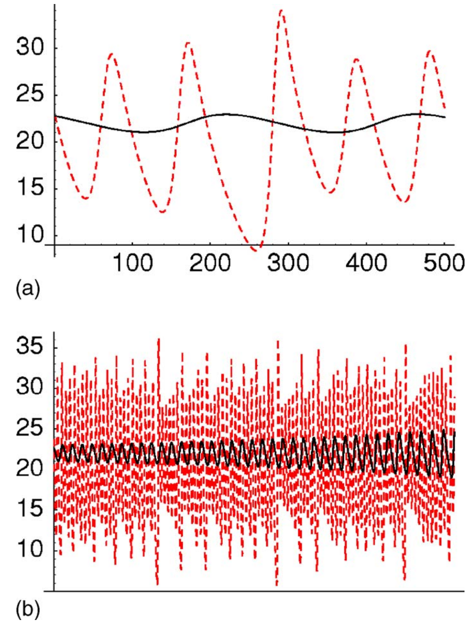

FIG. 39. (Color online) Evolution of z from Lorenz equations. Original, red dashed; perturbed, solid black. (a) Short term (500 steps), z. (b) Long term (10000 steps), z.

- The stability of a low-dimensional model is connected to its minimal representation. Often higher modes are incorporated to see if they can contribute to stability. The addition of these modes increases the dimensionality of the system and can introduce erroneous conclusions about minimal representations, bifurcations, stable and unstable manifolds and equilibria. The incorporation of higher modes for stability reasons, can also erroneously influence our conclusions about spatial structures that are participating in the dynamics.

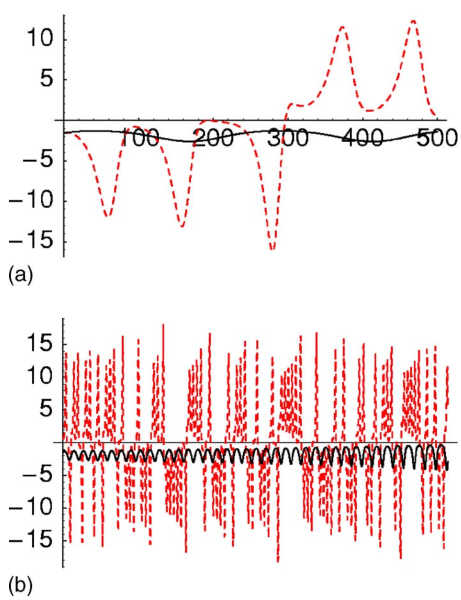

FIG. 38. (Color online) Evolution of y from Lorenz equations. Original, red dashed; perturbed, solid black. (a) Short term (500 steps), y. (b) Long term (10000 steps), y.

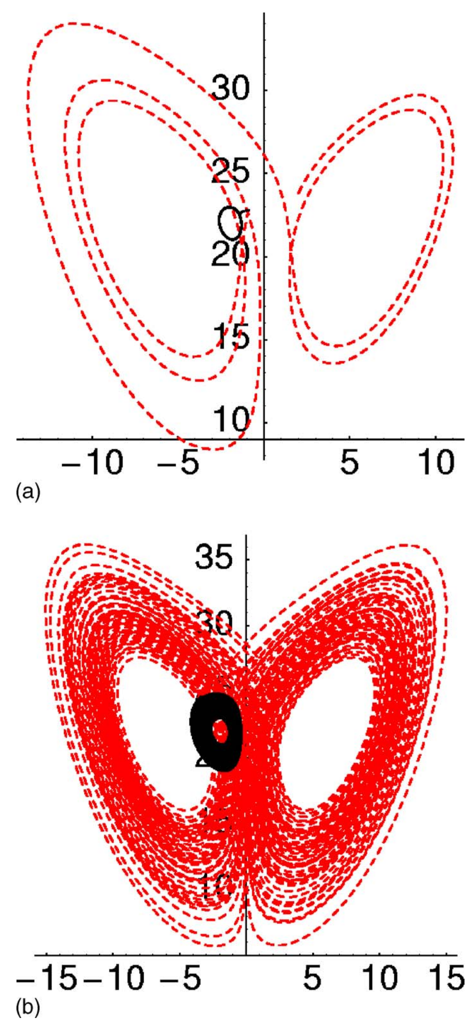

FIG. 40. (Color online) x-z phase portrait from Lorenz equations. Original, red dashed; perturbed, solid black. (a) Short term (500 steps), x vs z. (b) Long term (10000 steps), x vs z.

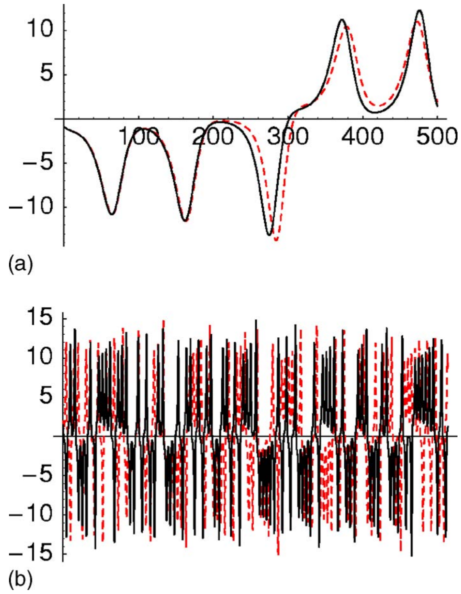

FIG. 41. (Color online) Evolution of x from Lorenz equations. Original, red dashed; corrected, solid black. (a) Short term (500 steps), x. (b) Long term (10000 steps), x.

- Stabilization schemes that incorporate *ad hoc* assumptions introduce additional physics that are simply not present in either the data or the procedure. While they may be justifiable due to knowledge the modeler has from fluid physics, it is inconsistent with the NS $\rightarrow$ POD $\rightarrow$ low-dimensional model.

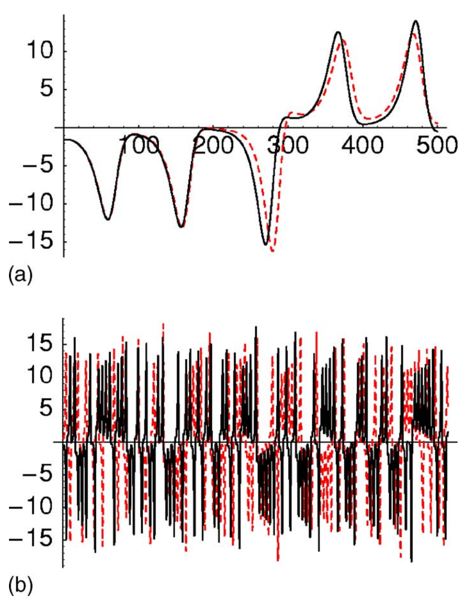

FIG. 42. (Color online) Evolution of y from Lorenz equations. Original, red dashed; corrected, solid black. (a) Short term (500 steps), y. (b) Long term (10000 steps), y.

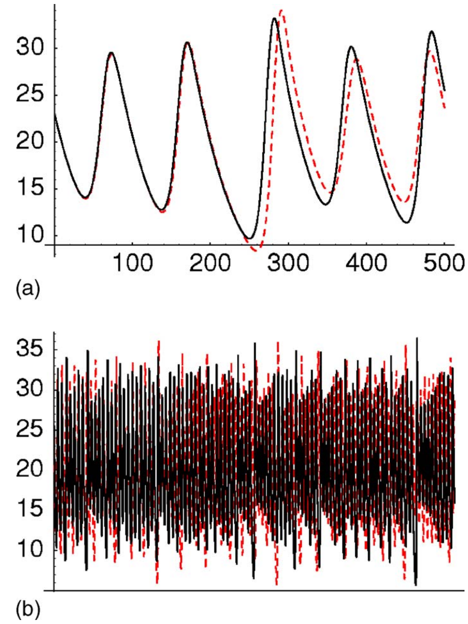

FIG. 43. (Color online) Evolution of z from Lorenz equations. Original, red dashed; corrected, solid black. (a) Short term (500 steps), z. (b) Long term (10000 steps), z.

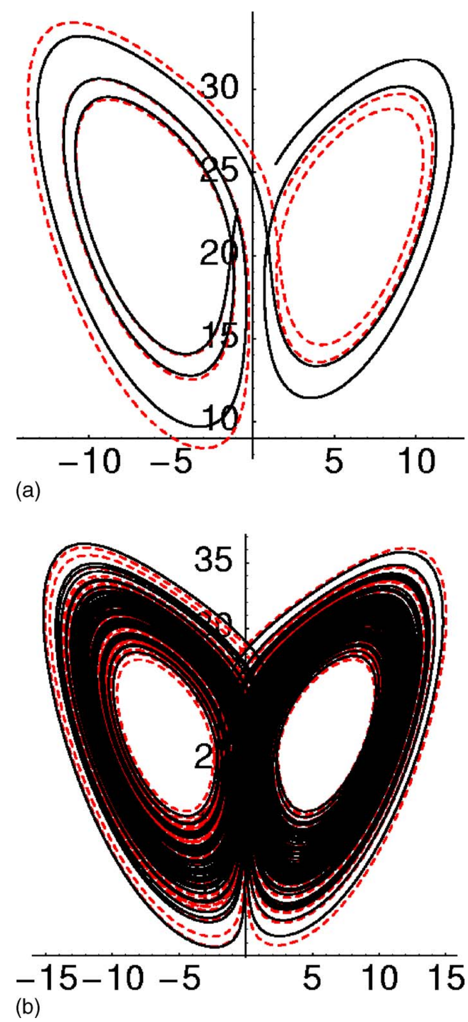

FIG. 44. (Color online) x-z phase portrait from Lorenz equations. Original, red dashed; corrected, solid black. (a) Short term (500 steps), x vs z. (b) Long term (10000 steps), x vs z.

ACKNOWLEDGMENT

V.L.K. thanks NASA Goddard Space Flight Center for support for this work which contributed to her Ph.D.

[1] P. Holmes, J. L. Lumley, and G. Berkooz, *Turbulence, Coherent Structures, Dynamical Systems and Symmetry* (Cambridge University Press, Cambridge, UK, 1996).

[2] D. Rempfer, "On low-dimensional Galerkin models for fluid flow," Theor. Comput. Fluid Dyn. **14**, 75 (2000).

[3] A. K. Bangia, P. F. Batcho, I. G. Kevrekidis, and G. E. Karniadakis, "Unsteady two-dimensional flows in complex geometries: comparative bifurcation studies with global eigenfunction expansions," SIAM J. Sci. Comput. (USA) **18**, 775 (1997).

[4] B. H. Jørgensen, "Low-dimensional modeling of a driven cavity flow with two free parameters," Theor. Comput. Fluid Dyn. **16**, 299 (2003).

[5] B. R. Noack, K. Afansiev, M. Morzynski, G. Tadmor, and F. Thiele, "A hierarchy of low-dimensional models for the transient and post-transient cylinder wake," J. Fluid Mech. **497**, 335 (2003).

[6] V. Kalb, "Low-dimensional models for fluid flow," Ph.D. dissertation, University of Maryland, College Park, MD (2004).

[7] J. L. Lumley, "The structure of inhomogeneous turbulent flows," in *Atmospheric Turbulence and Radio Wave Propagation*, edited by A. M. Yaglom and V. L. Tararsky (Nauka, Moscow, 1967), pp. 166–178.

[8] K. Karhunen, "Zur Spektraltheorie stochastischer Prozesse," Ann. Acad. Sci. Fenn., Ser. A1: Math.-Phys. **37**, 1 (1946).

[9] M. M. Loève, *Probability Theory* (Van Nostrand, Princeton, NJ, 1955).

[10] Y. C. Liang, H. P. Lee, S. P. Lim, W. Z. Lin, K. H. Lee, and C. G. Wu, "Proper orthogonal decomposition and its applications, part I: theory," J. Sound Vib. **252**, 527 (2002).

[11] M. Rathinam and L. R. Petzold, "A new look at proper orthogonal decomposition," SIAM (Soc. Ind. Appl. Math.) J. Numer. Anal. **41**, 1893 (2003).

[12] C. López and E. Hernández-García, "Low-dimensional dynamical system model for observed coherent satellite data," Physica A **328**, 233 (2003).

[13] W. R. Graham, J. Peraire, and K. Y. Tang, "Optimal control of vortex shedding using low order models: Part I: Open-loop model development," Int. J. Numer. Methods Eng. **44**, 945 (1999).

[14] E. A. Gillies, "Low-dimensional control of the circular cylinder wake," J. Fluid Mech. **371**, 157 (1998).

[15] L. Sirovich, "Turbulence and the dynamics of coherent structures part I: coherent structures," Q. Appl. Math. **45**, 561 (1987).

[16] N. Aubry, "On the hidden beauty of the proper orthogonal decomposition," Theor. Comput. Fluid Dyn. **2**, 339 (1991).

[17] A. E. Deane, I. G. Kevrekidis, G. E. Karniadakis, and S. A. Orszag, "Low-dimensional models for complex geometry flow: application to grooved channels and circular cylinders," Phys. Fluids A **3**, 2337 (1991).

[18] A. Sohankar, C. Norberg, and L. Davidson, "Simulation of three-dimensional flow around a square cylinder at moderate Reynolds numbers," Phys. Fluids **11**, 288 (1999).

[19] L. Prandtl, *Essentials of Fluid Dynamics* (Hafner, New York, 1953).

[20] W. Cazemier, R. W. C. P. Verstappen, and A. E. P. Veldman, "Proper orthogonal decomposition and low-dimensional models for driven cavity flows," Phys. Fluids **10**, 1685 (1998).

[21] A. J. Chorin, "Numerical solution of the Navier-Stokes equations," Math. Comput. **22**, 745 (1968).

[22] M. Griebel, T. Dormseifer, and T. Neunhoeffer, *Numerical Simulation in Fluid Dynamics* (SIAM, Philadelphia, 1998).

[23] F. Harlow and J. Welch, "Numerical calculation of time-dependent viscous incompressible flow of fluid with free surface," Phys. Fluids **8**, 2182 (1965).

[24] J. Kim and P. Moin, "Application of a fractional step method to incompressible Navier-Stokes equations," J. Comput. Phys. **59**, 308 (1985).

[25] U. Ghia, K. N. Ghia, and C. T. Shin, "High-Re solutions for incompressible flow using the Navier-Stokes equations and a multigrid method," J. Comput. Phys. **48**, 387 (1982).

[26] O. Botella and R. Peyret, "Benchmark spectral results on the lid-driven cavity flow," Comput. Fluids **27**, 421 (1998).

[27] C. W. Oosterlee, P. Wesseling, A. Segal, and E. Brakkee, "Benchmark solutions for the incompressible Navier-Stokes equations in general coordinates on staggered grids," Int. J. Numer. Methods Fluids **17**, 301 (1993).

[28] P. M. Gresho, D. K. Gartling, J. R. Torczynski, K. A. Cliffe, K. H. Winters, T. J. Garratt, A. Spence, and J. W. Goodrich, "Is the steady viscous incompressible two-dimensional flow over a backward-facing step at Re800 stable," Int. J. Numer. Methods Fluids **17**, 501 (1993).

[29] G. E. Karniadakis, M. Israeli, and S. A. Orszag, "High-order splitting methods for the incompressible Navier-Stokes equations," J. Comput. Phys. **97**, 414 (1991).

[30] B. Galletti, C. H. Bruneau, L. Zannetti, and A. Iollo, "Low-order modelling of laminar flow regimes past a confined square cylinder," J. Fluid Mech. **503**, 161 (2004).

[31] B. R. Noack, P. Papas, and P. A. Monkewitz, "The need for a pressure-term representation in empirical Galerkin models of incompressible shear flows," J. Fluid Mech. **523**, 339 (2005).

[32] M. Marion and R. Temam, "Nonlinear Galerkin methods," SIAM (Soc. Ind. Appl. Math.) J. Numer. Anal. **26**, 1139 (1989).

[33] S. Sirisup and G. E. Karniadakis, "A spectral viscosity method for correcting the long-term behavior of POD models," J. Comput. Phys. **194**, 92 (2004).

[34] B. Podvin and P. Le Quéré, "Low-order models for the flow in a differentially heated cavity," Phys. Fluids **13**, 3204 (2001).

[35] X. Ma and G. E. Karniadakis, "A low-dimensional model for simulating 3D cylinder flow," J. Fluid Mech. **458**, 181 (2002).

[36] E. Tadmor, "Convergence of spectral methods for nonlinear conservation laws," SIAM (Soc. Ind. Appl. Math.) J. Numer. Anal. **26**, 30 (1989).

[37] E. J. Doedel, A. R. Champneys, T. F. Fairgrieve, Y. A. Kuznetsov, B. Sandstede, and X. Wang, "AUTO 97: Continuation and bifurcation software for ordinary differential equations (with HomCont)," http://indy.cs.concordia.ca/auto (1998).

[38] K. T. Alligood, T. D. Sauer, and J. A. Yorke, *CHAOS: An Introduction to Dynamical Systems* (Springer-Verlag, New York, 1996).